S-matrix-based bandpass negative group delay innovative model of inverted parallel arm distributed topology

Samuel Ngoho, Mariam Deme Camara, Yuandan Dong, Alexandre Douyère, Nour Mohammad Murad, Preeti Thakur, Atul Thakur, Rivo Randriatsiferana, Blaise Ravelo

S-matrix based bandpass negative group delay innovative model of inverted parallel arm distributed topology

Samuel Ngoho[1], Mariam Dème Camara[2], Yuandan Dong[3], Alexandre Douyère[4], Nour Mohammad Murad[4], Preeti Thakur[5], Atul Thakur[5], Rivo Randriatsiferana[6] and Blaise Ravelo[7]

[1] *Association Française de Science des Systèmes (AFSCET), Paris, France*

[2] *ISEP-Institut Supérieur d'Électronique de Paris, 10 rue de Vanves, Issy les Moulineaux, 92130-France*

[3]*Univ. of Electronic Science and Technology of China, School of Electronic Science and Engineering, China*

[4] *Energy Lab, Institut Universitaire de Technologie, University of La Reunion, Saint Pierre 97410, France*

[5] *Amity University Haryana, Gurgaon, 122413 India*

[6] *University of Rennes 1, CNRS, IETR-UMR 6164, F-35000 Rennes, France*

[7] *Nanjing University of Information Science & Technology (NUIST), Nanjing, Jiangsu 210044, China*

E-mail: samngoho@yahoo.fr, mariam.camara@isep.fr, ydong@uestc.edu.cn, alexandre.douyere@univ-reunion.fr, nour.murad@univ-reunion.fr, pthakur@ggn.amity.edu, athakur1@ggn.amity.edu, rivo.randriatsiferana@univ-rennes1.fr, blaise.ravelo@yahoo.fr

Corresponding author: Rivo Randriatsiferana

e-mail: rivo.randriatsiferana@univ-rennes1.fr

S-matrix based bandpass negative group delay innovative model of inverted parallel arm distributed topology

This paper develops an innovative model of bandpass (BP) negative group delay (NGD) inverted arm topology of parallel lines. The S-matrix model is established from impedance and admittance matrix operations of elementary transmission lines (TLs) constituting the topology. Parametric analysis is performed to assess the influence of inverted arm structure sizes on the BP NGD specifications. To validate the theoretical concept, a proof of concept (POC) is designed in microstrip technology. The calculated and simulated results are in very good agreement. NGD value, center frequency and bandwidth of about -8 ns, 3.6 GHz and 4 MHz, respectively, are observed with insertion loss better than 1 dB and reflection loss better than 18 dB. The innovative NGD physical structure could be an important asset to reduce propagation delay in the upcoming telecommunications systems as the 5G system.

Keywords: Bandpass (BP) negative group delay (NGD), NGD topology, transmission line (TL), S-matrix modelling.

1. Introduction

Current research progress on RF and microwave device designs for the communication system performance improvement lead to the development of oscillators [1], non-Foster element [2] and group delay equalizer [3-4] operating with the unfamiliar bandpass (BP) negative group delay (NGD) function. The NGD function was initially experimented in optical wavelength in 1980s [5-6]. However, because of its counterintuitive effect, the NGD function remains an unfamiliar and closed topic for most of electronic, RF and microwave engineers. So far, one of fundamental NGD interpretations is the effect of positive and negative interferences between waves propagating through two parallel ways [5-10]. The mechanism of this NGD effect was verified experimentally in optical [5,7] and microwave wavelengths [8-10]. But similar to classical electronic functions, the diversity of BP NGD function was also revealed

with unforecasted microwave circuits [11-22]. In 2000s, the identification of BP NGD function has been profitably made during the metamaterial revolution in the area of microwave engineering [11-13]. The NGD effect was mathematically understood from the possibility to generate negative refractive index which is naturally associated to the negative group velocity (NGV) [11-13]. The NGD function can also be generated with absorptive filter aspect [14]. However, further research work must be made to reduce the BP NGD circuit attenuation loss and the physical size. In 2010s, novel designs of compact BP NGD circuits were proposed [15-19]. The generation of these compact NGD microwave circuits [15-19] were implemented with microstrip transmission lines (TLs). Despite the diversity of NGD topologies, the interpretation and familiarity are not open enough to many RF and microwave non-specialist engineers. Until now, the easiest way to understand the NGD theory is based on the analogy with the linear filter function [20-21]. According to the NGD frequency bands, we can classify the low-pass [20-23], high-pass [20-21,24-25], and BP NGD functions [12-21,26-27].

But the NGD analysis with respect to the physical effect requires further research effort. For this reason, the present work explains the BP NGD illustration with inverted arm two-port topology composed of different TLs $TL_{\zeta=\{x,y\}}(Z_\zeta,d_\zeta)$ with characteristic impedance, Z_ζ, and physical length, d_ζ, shown in Fig. 1.

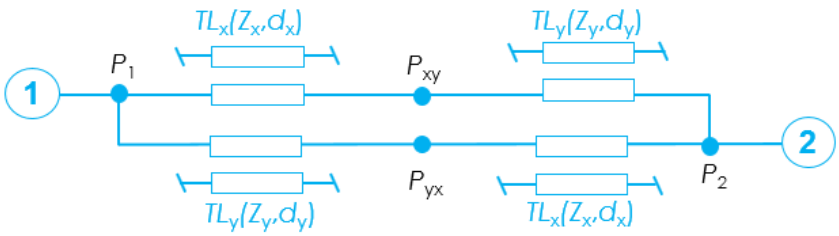

Figure 1. Two-ports inverted arm topology.

In difference to the two cells-based BP NGD analysis introduced in [27], the BP NGD topology originality lies on the fact that the BP NGD function can also be generated even if the TLs constituting the arms present the same characteristic impedance and

physical lengths. The paper is organized in three sections. Section 2 focuses on the theoretical analysis NGD behavior of the structure. The S-matrix model based on impedance (Z-) and admittance (Y-) matrix operations is established. Section 3 is the validation results with a BP NGD inverted arm circuit as a proof of concept (POC). The section includes the parametric study of the POC constitutive geometrical characteristics. Lastly, Section 4 is the paper conclusion.

2. *S-matrix model of inverted parallel arm topology*

The analytical S-matrix modelling between access ports ① and ②, of the inverted arm topology shown in Fig. 1 is developed in the present section.

2.1 Analytical operation with Z- and Y-matrix

The Z-matrix based equivalent diagram of the inverted arm topology is represented by Fig. 2(a). With the generalized index, $\zeta=\{x,y\}$, the model is elaborating by considering characteristic impedance, $Z_\zeta(j\omega)$, and the constant propagation:

$$\gamma_\zeta(j\omega)=\alpha_\zeta(\omega)+j\beta_\zeta(\omega) \tag{1}$$

by denoting $\alpha_\zeta(\omega)$ and $\beta_\zeta(\omega)$ the attenuation and phase constants with the angular frequency, ω. The elementary Z-matrix is given by:

$$[Z^\zeta(j\omega)]=\begin{bmatrix} Z_{1\zeta}(j\omega) & Z_{2\zeta}(j\omega) \\ Z_{2\zeta}(j\omega) & Z_{1\zeta}(j\omega) \end{bmatrix}=Z_\zeta\begin{bmatrix} 1/\tanh\left[\gamma_\zeta(\omega)d_\zeta\right] & 1/\sinh\left[\gamma_\zeta(\omega)d_\zeta\right] \\ 1/\sinh\left[\gamma_\zeta(\omega)d_\zeta\right] & 1/\tanh\left[\gamma_\zeta(\omega)d_\zeta\right] \end{bmatrix} \tag{2}$$

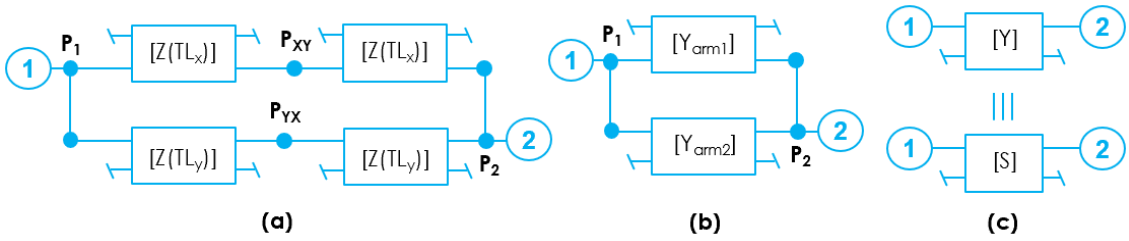

Figure 2. (a) Z-, (b) reduced two-arm Y- and (c) global Y and S matrix block diagrams.

Based on the circuit and system theory, we have the following equation system related to the cascade of $\left[Z^x(j\omega)\right]$ and $\left[Z^y(j\omega)\right]$:

$$\begin{cases} \begin{bmatrix} V_{1x} \\ V_{2x} \end{bmatrix} = \begin{bmatrix} Z_{1x}(j\omega) & Z_{2x}(j\omega) \\ Z_{2x}(j\omega) & Z_{1x}(j\omega) \end{bmatrix} \times \begin{bmatrix} I_{1x} \\ I_{2x} \end{bmatrix} \\ \begin{bmatrix} V_{1y} \\ V_{2y} \end{bmatrix} = \begin{bmatrix} Z_{1y}(j\omega) & Z_{2y}(j\omega) \\ Z_{2y}(j\omega) & Z_{1y}(j\omega) \end{bmatrix} \times \begin{bmatrix} I_{1y} \\ I_{2y} \end{bmatrix} \\ I_{2x} = -I_{1y} \\ V_{2x} = V_{1y} \end{cases} \tag{3}$$

By eliminating I_{2x}, I_{1y}, V_{2x} and V_{1y}, it can be established that the equivalent Z-matrix of cascaded $\left[Z^x(j\omega)\right]$ and $\left[Z^y(j\omega)\right]$ is defined analytically by:

$$\begin{bmatrix} V_{1x} \\ V_{2y} \end{bmatrix} = [Z^{xy}] \times \begin{bmatrix} I_{1x} \\ I_{2y} \end{bmatrix} \Leftrightarrow \begin{cases} V_{1x} = Z_{11}^{xy} I_{1x} + Z_{12}^{xy} I_{2y} \\ V_{2y} = Z_{21}^{xy} I_{1x} + Z_{22}^{xy} I_{2y} \end{cases} \tag{4}$$

After identification of currents I_{1x} and I_{2y}, from previous system, it yields the Z-matrices of each arm represented in Fig. 2(b) expressed as:

$$[Z^{xy}] = \begin{bmatrix} Z_{11}^{xy} & Z_{12}^{xy} \\ Z_{21}^{xy} & Z_{22}^{xy} \end{bmatrix} = \frac{\begin{bmatrix} Z_{1x}(j\omega)\left[Z_{1x}(j\omega) + Z_{1y}(j\omega)\right] & Z_{2x}(j\omega)Z_{2y}(j\omega) \\ -Z_{2x}^2(j\omega) & \\ Z_{2x}(j\omega)Z_{2y}(j\omega) & Z_{1y}(j\omega)\left[Z_{1x}(j\omega) + Z_{1y}(j\omega)\right] \\ & -Z_{2y}^2(j\omega) \end{bmatrix}}{Z_{1x}(j\omega) + Z_{1y}(j\omega)} \tag{5}$$

$$[Z^{yx}] = \begin{bmatrix} Z_{11}^{yx} & Z_{12}^{yx} \\ Z_{21}^{yx} & Z_{22}^{yx} \end{bmatrix} = \frac{\begin{bmatrix} Z_{2x}(j\omega)\left[Z_{2x}(j\omega) + Z_{2y}(j\omega)\right] & Z_{1x}(j\omega)Z_{1y}(j\omega) \\ -Z_{1x}^2(j\omega) & \\ Z_{1x}(j\omega)Z_{1y}(j\omega) & Z_{2y}(j\omega)\left[Z_{2x}(j\omega) + Z_{2y}(j\omega)\right] \\ & -Z_{1y}^2(j\omega) \end{bmatrix}}{Z_{1x}(j\omega) + Z_{1y}(j\omega)}$$

(6)

2.2 Y-matrix equivalent model of the inverted-arm topology

The inverse matrices of $[Z^{xy}]$ and $[Z^{yx}]$ in equations (5) and (6), respectively, are given by the following arm Y-matrices:

$$\left[Y_{arm_1}(j\omega)\right]=\frac{\begin{bmatrix} Z_{22}^{xy}(j\omega) & -Z_{21}^{xy}(j\omega) \\ -Z_{21}^{xy}(j\omega) & Z_{11}^{xy}(j\omega) \end{bmatrix}}{Z_{11}^{xy}(j\omega)^2-Z_{21}^{xy}(j\omega)^2} \tag{7}$$

$$\left[Y_{arm_2}(j\omega)\right]=\frac{\begin{bmatrix} Z_{22}^{yx}(j\omega) & -Z_{21}^{yx}(j\omega) \\ -Z_{21}^{yx}(j\omega) & Z_{11}^{yx}(j\omega) \end{bmatrix}}{Z_{11}^{yx}(j\omega)^2-Z_{21}^{yx}(j\omega)^2} \tag{8}$$

The global Y-matrix presented in Fig. 2(c) can therefore be expressed as:

$$\left[Y(j\omega)\right]=\left[Y_{arm_1}(j\omega)\right]+\left[Y_{arm_2}(j\omega)\right] \tag{9}$$

2.3 S-matrix equivalent model of the inverted arm topology

Acting as a symmetric passive topology, the 2-D equivalent S-matrix of the inverted arm topology shown in Fig. 1 presents reflection and transmission coefficients: S_{11}=S_{22} and S_{12}=S_{21}, respectively. By denoting the reference impedance, R_0=50 Ω, the inverted arm topology global S-matrix can be derived from Y-to-S transform relationship:

$$\left[S(j\omega)\right]=\begin{bmatrix} S_{11}(j\omega) & S_{21}(j\omega) \\ S_{21}(j\omega) & S_{11}(j\omega) \end{bmatrix}=\begin{Bmatrix} \left\{\begin{bmatrix} 1 & 0 \\ 0 & 1 \end{bmatrix}/R_0-\left[Y_{arm_1}(j\omega)\right]-\left[Y_{arm_2}(j\omega)\right]\right\}\times \\ \left\{\begin{bmatrix} 1 & 0 \\ 0 & 1 \end{bmatrix}/R_0+\left[Y_{arm_1}(j\omega)\right]+\left[Y_{arm_2}(j\omega)\right]\right\}^{-1} \end{Bmatrix} \tag{10}$$

The GD of the inverted arm network can be computed from the transmission coefficient by means of the following definition:

$$GD(\omega)=-\partial\arg\left[S_{21}(j\omega)\right]/\partial\omega \tag{11}$$

To verify that the inverted arm topology behaves as a BP NGD circuit, applicative study showing the existence of microwave frequency, ω_n with:

$$GD_n = GD(\omega_n) < 0 \quad (12)$$

must be performed. The design phase of the POC circuit based on microstrip topology will be described in the next paragraph.

2.4 NGD design method of inverted-arm microstrip circuit

Similar to classical microwave passive circuits as filter, power divider/combiner, and coupler, the inverted arm NGD circuit can be designed in five successive steps as described in Fig. 3. The main tasks constituting the different steps are explained. First, the NGD specifications are chosen. Then, considering the topology introduced in Fig.1, the inverted arm TL characteristics are calculated. The parametric analysis and optimization are performed to take into account the microstrip TL imperfections. Finally, the validation with the GD and S-parameter responses is fulfilled.

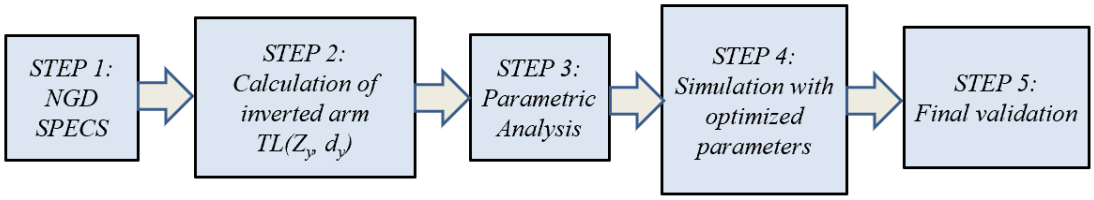

Figure 3. Inverted arm topology-based BP NGD circuit design flow

Next section focuses on the BP NGD behavioral feasibility within the inverted-arm topology. A POC allowing to analysis the GD and S-matrix responses is examined.

3. *Realistic investigation and validation results*

This section aims to validate the BP NGD behavior of the inverted arm topology introduced in Fig. 1 and developed in the previous section. The POC parametric description is investigated with respect to the circuit physical sizes. Then, the theoretical calculations based on S-parameters and simulations from ADS® environment, are compared and discussed.

3.1 Description of the POC microstrip circuit

The POC microstrip circuit design was carried out under the desired specifications of the BP NGD function indicated in Table 1. The ADS schematic model of the inverted arm circuit under study is illustrated by Fig. 4(a). The POC consists of two identical horizontal TL elements characterized by width, w_1 and length, d_1; and two identical vertical TL elements identified by width, w_2 and length, d_2.

Center frequency (f_n)	**NGD value (GD_n)**	**NGD bandwidth (Δf_n)**	**Insertion loss $S_{21dB}(f_n)$**	**Reflection coefficient $S_{11dB}(f_n)$**
f_1=3.6 GHz	-10 ns	10 MHz	-1 dB	-10 dB

Table 1: BP NGD specifications

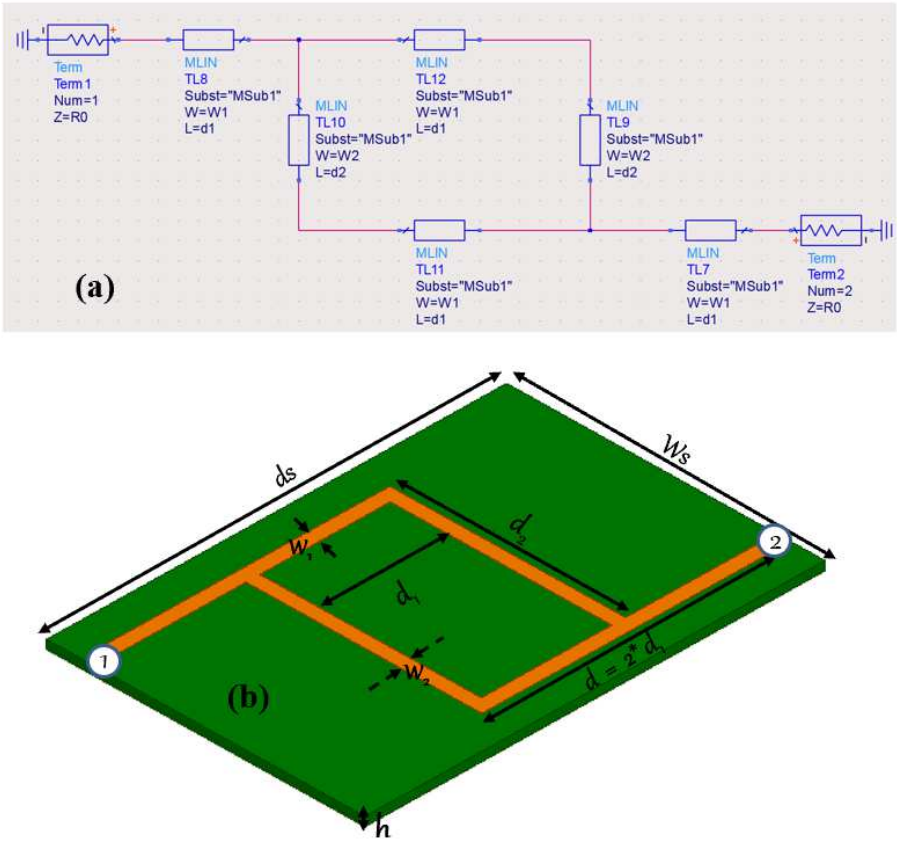

Figure 4. (a) ADS® scheme and (b) 3-D design of the parallel inverted arm circuit POC

These physical dimensions were determined from the Hammerstad-Jensen model [28] in function of the expected BP NGD specifications by means of the NGD center

frequencies, characteristic impedances and electrical lengths. The 3-D design of the inverted arm circuit POC is shown in Fig. 4(b). Port ① and port ② are the POC circuit main accesses. This POC is implemented on substrate ROGERS Duroid 5870 with relative permittivity, ε_r=2.33, and loss tangent, tan (δ)=0.0012. The metallization is constituted by Copper metal having thickness, t=35 µm. The POC circuit physical and electrical parameters are summarized in Table 2.

Type	**Description**	**Name**	**Value**
Circuit	Length	d_1	32 mm → 38 mm
		d_2	26 mm → 30 mm
	Width	w_1	3 mm → 5 mm
		w_2	1 mm → 2 mm
Materials	**Properties**	**Name**	**Value**
ROGERS duroid 5870 Substrate	Relative permittivity	ε_r	2.33
	Loss tangent	tan(δ)	0.0012
	Height	h	1.6 mm
Metallization	Thickness	t	35 µm
	Conductivity	σ	58 MS/s

Table 2: Substrates and physical parameters of the inverted arm circuit POC

3.2 Parametric analyses with respect to the inverted-arm circuit physical sizes

The proposed parametric analysis enables to assess the influence of the inverted-arm circuit physical parameters on the BP NGD responses. It is based on the analysis of the S-parameters model and simulation with the commercial tool ADS® from Keysight Technologies®.

3.2.1 Parametric analysis with respect to w_1

Fig. 5 presents the *GD*, S_{21}, and S_{11} mappings of the inverted-arm NGD POC versus w_1 and frequency from 3.595 GHz to 3.62 GHz. The investigation was performed with w_1 varied linearly from 3 mm to 5 mm. Fig. 5(a) highlights that the POC presents a BP NGD behavior in the considered range of w_1. It can be emphasized that the NGD absolute value increases with w_1. Fig. 5(d) shows that the NGD center frequency

increases when w_1 increases. As seen in Fig. 5(b) that S_{21} and GD present a similar behavior with maximal insertion loss changing from about -2.5 dB to -0.5 dB. The cartography of S_{11} shown in Fig. 5(c) show that the POC circuit is well-matched in the range of considered w_1.

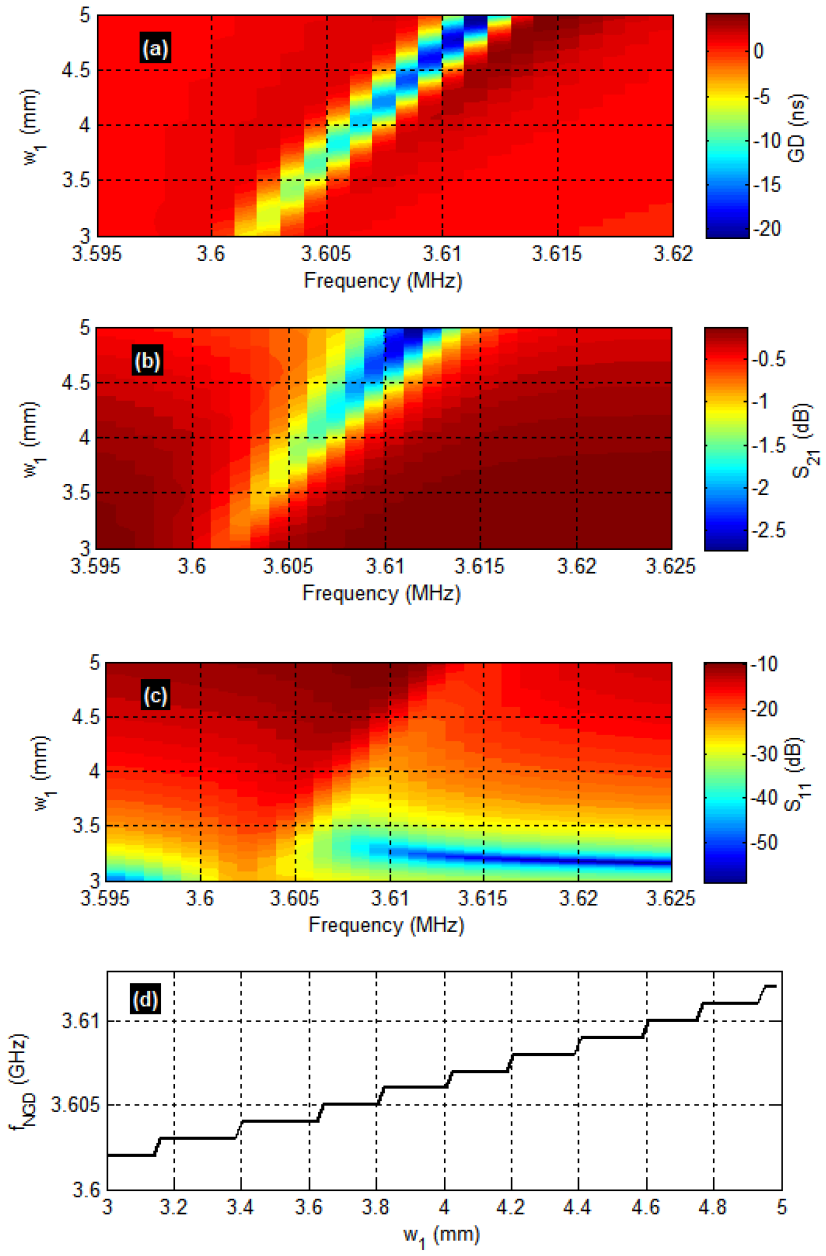

Figure 5. Mappings of (a) *GD*, (b) S_{21} and (c) S_{11} vs (f, w_1), and (d) f_{NGD} vs w_1.

3.2.2 Parametric analysis with respect to w_2

In this case, the S-parameter parametric analysis was performed versus w_2 which is varied from 1 mm to 2 mm. The *GD*, S_{21}, and S_{11} responses are mapped in Figs. 6(a), 6(b) and 6(c), respectively. Once again, the inverted-arm topology behaves as a BP NGD function in the range of w_2. As depicted in Fig. 6(a), the GD minimal value tends to increase when w_2 is higher.

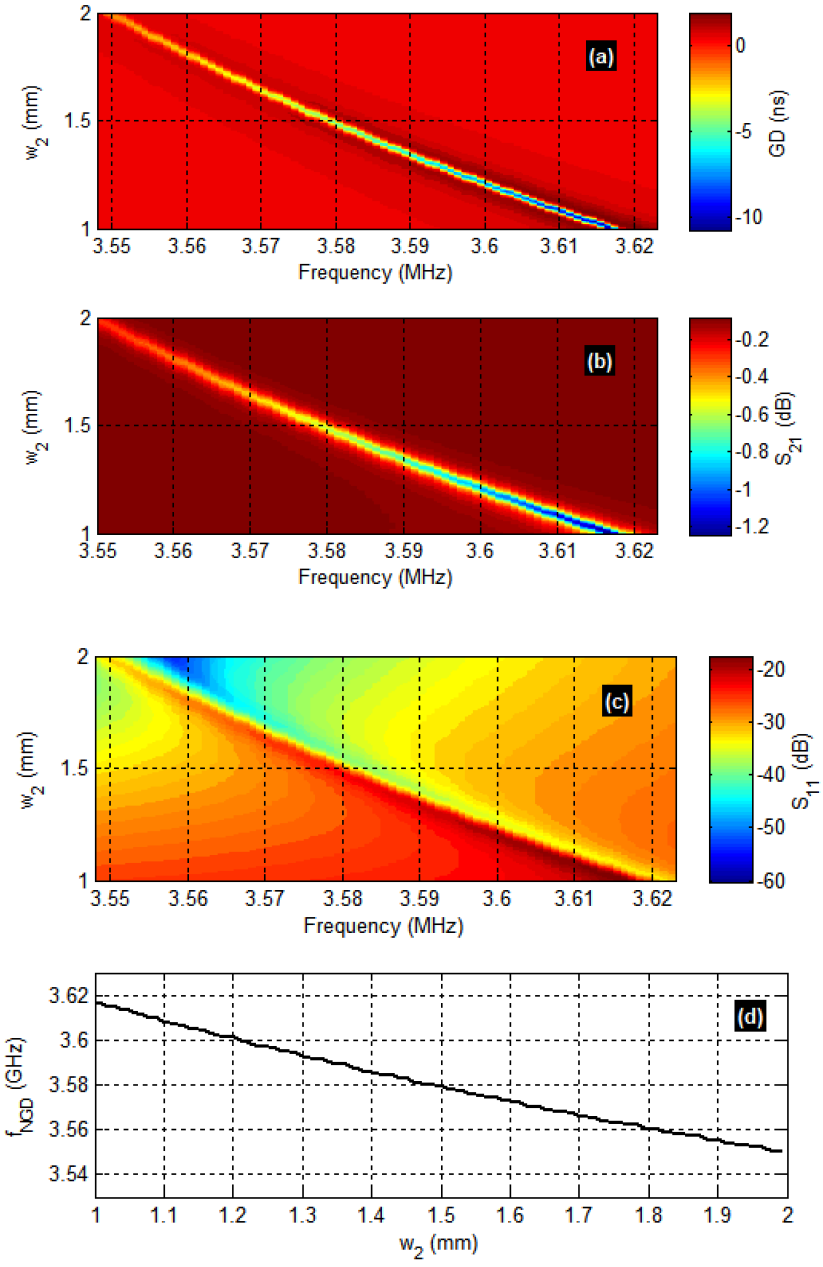

Figure 6. Mappings of (a) *GD*, (b) S_{21} and (c) S_{11} vs (f, w_2) and (d) f_{NGD} vs w_2.

In this case, the NGD center frequency, plotted in Fig. 6(d) decreases from about 3.62 GHz to 3.53 GHz. Fig. 6(b) represents the S_{21} mapping. As we can see, in Fig. 6(f), it reaches its minimum when w_2 is higher. Fig. 6(c) show the S_{11} cartography. It can be emphasized that the POC circuit access matching can be better than -20 dB in the considered range of w_2.

3.2.3 Parametric analysis with respect to d_1

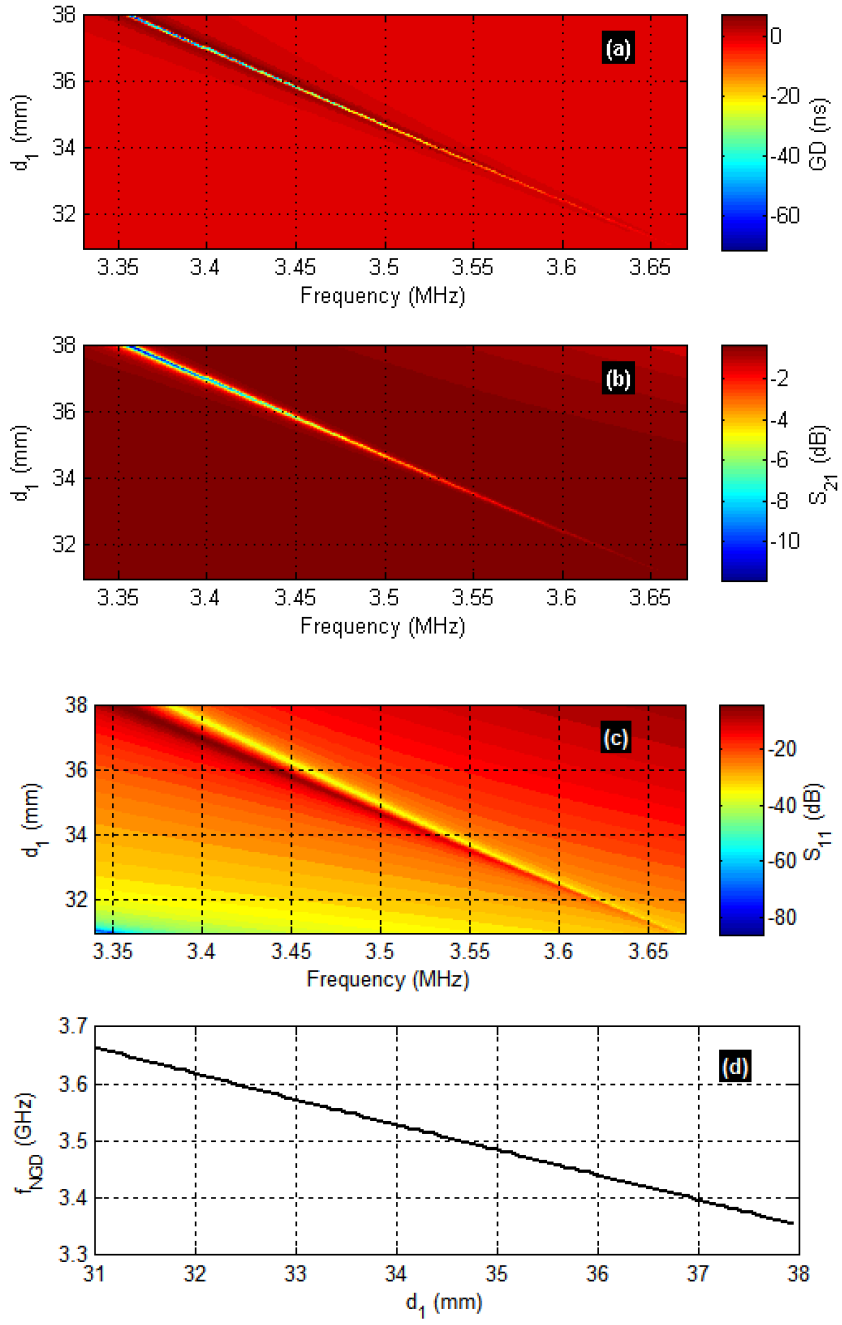

Figure 7. Mappings of (a) *GD*, (b) S_{21} and (c) S_{11} vs (f, d_1) and (d) f_{NGD} vs d_1.

This third case of parametric study was carried by linearly varying d_1 from 32 mm to 38 mm. Figs. 7(a), 7(b) and 7(c) depict the *GD*, S_{21}, and S_{11} mappings versus frequency and d_1, respectively. It can be observed in Fig. 7(a) that the inverted-arm topology under study still behaves as a BP NGD function in the considered range of physical length, d_1. Furthermore, the NGD minimal absolute value increases from some nanoseconds to several tens of nanoseconds with d_1. The NGD center frequency plotted in Fig. 7(d) decreases from 3.65 GHz to 3.35 GHz when d_1 varies between 32 mm to 38 mm. The mappings of Figs. 7(b) and Fig. 7(c) highlight the behavior of the transmission and reflection losses, respectively. It can be concluded that the attenuation and reflection losses are worst when d_1 increases.

3.2.4 Parametric analyses with respect to d_2

Figs. 8(a), 8(b) and 8(c) display the mappings of *GD*, S_{21} and S_{11} in function of d_2 and frequency. In this last parametric analysis, d_2 varies linearly from 26 mm to 30 mm and the frequency range is delimited between 3.45 GHz and 3.95 GHz. As depicted in Fig. 8(a), the BP NGD behavior is not conserved despite the variation of d_2 and the GD minimal value increases when d_2 decreases. Based on the plot of Fig. 8(d), the NGD center frequency is shifted between 3.95 GHz and 3.45 GHz in the considered range of d_2. The cartography of S_{21} in Fig. 8(b) shows how transmission losses increase when d_2 decreases. Fig. 8(c) presents the S_{11} mapping. It can be seen that the reflection coefficient is more sensitive to d_2, the matching is degraded when d_2 is very large.

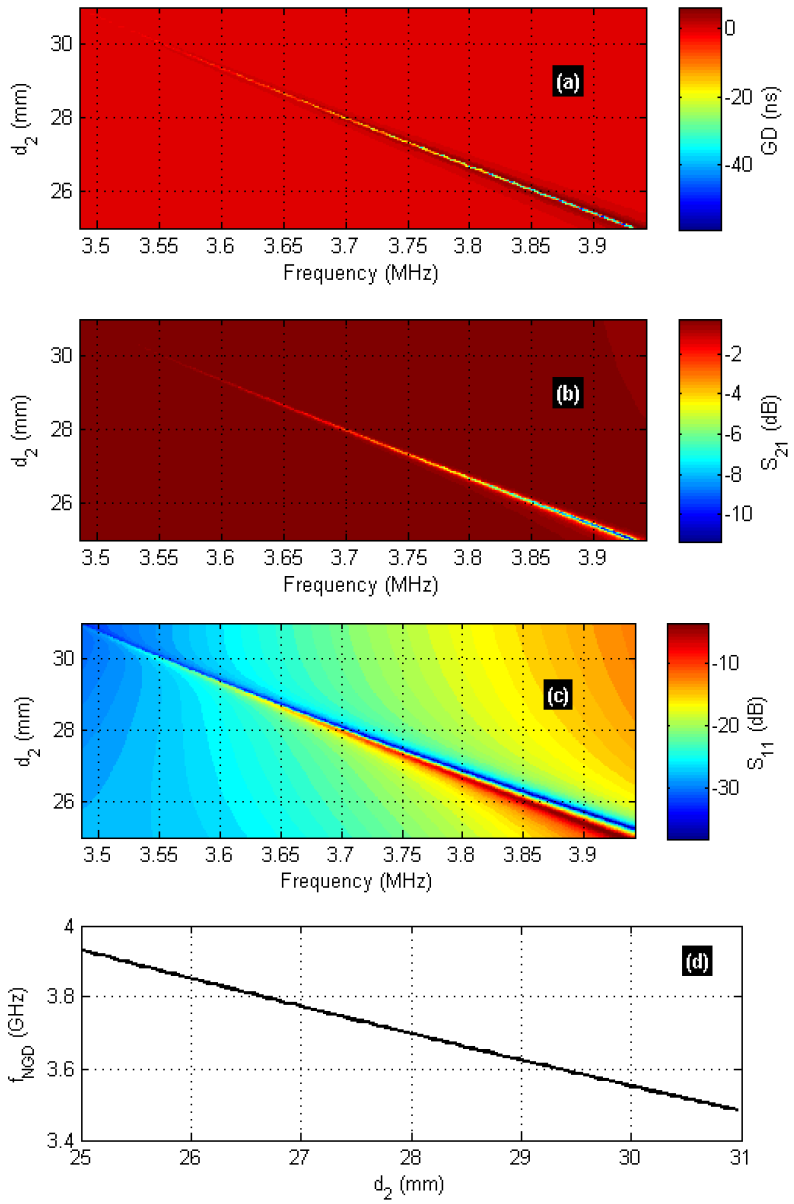

Figure 8. Mappings of (a) *GD*, (b) S_{21} and (c) S_{11} vs (f, d_2), and (d) f_{NGD} vs d_2.

3.3 Discussion on validation results

The previous parametric analysis highlighted the effect of the inverted arm circuit parameters on the BP NGD specifications. This study leads to the choice of optimal physical parameters of the inverted arm topology according to the previously given BP NGD specifications. Following, the theoretical model was calculated with MATLAB® via programming of analytical S-parameters established in equation (10). The simulated circuit was implemented with ADS® schematic environments from Keysight

Technologies® as shown in Fig. 4(a). The characteristics of the substrate and metallization are indicated in Table 2. The validation study was performed in the frequency band between 3.58 GHz and 3.62 GHz under 301 samplings. Figs. 9 compare the calculated and simulated GD, S_{21}, and S_{11} results. The red solid curves represent the theoretical model and the black solid ones represent the ADS® simulation result. As seen in Fig 9(a), the inverted-arm structure presents NGD BP responses for the two modelling cases. Nevertheless, as summarized in Table 3, slight discrepancies are observed on NGD minimal value, and NGD bandwidth.

Approach	Theory	Schematic
f_n	3.604 GHz	3.604 GHz
BW	1.7 MHz	3.3 MHz
GD_n	-9 ns	-8.699 ns
Computation duration	0.83 s	0.79 s

Table 3: Comparison of calculated and simulated NGD performances of the inverted-arm POC circuit.

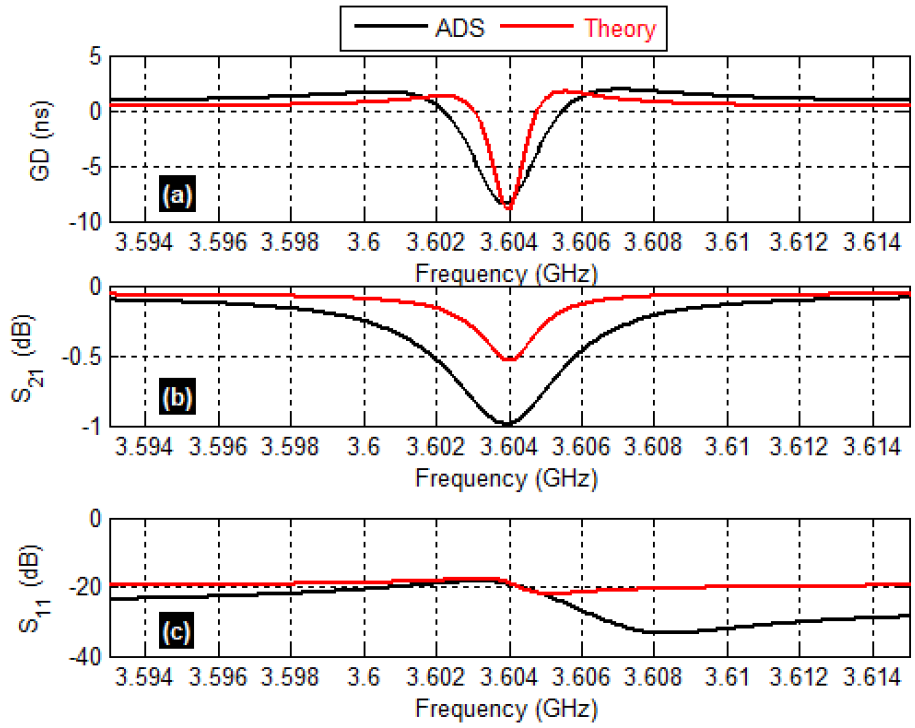

Figure 9. S-parameters comparison between theoretical model, and ADS schematic model: (a) *GD*, (b) S_{21} and (c) S_{11}.

These minimal differences are mainly due to the simplified theoretical model of the TL which does not take into account the numerical solver inaccuracies. In addition to the NGD aspect, the proposed BP NGD topology presents good performances in the NGD BW. The transmission losses displayed in Fig. 9(b) are widely better than -1 dB and the reflection coefficients are better lower than -20 dB.

3.4 State-of the-art comprehensive comparison of BP NGD performance

To answer to curious questions about the BP NGD performances of the inverted arm topology, a brief state of the art about the BP NGD passive circuits is revealed in the present subsection. The main parameters constituting the design challenge about BP NGD passive circuit are the center frequency, NGD value, NGD bandwidth, transmission and reflection coefficients. Table 4 indicates the established comprehensive comparison of BP NGD performances from the performed research work and available results in the literature [1,8-9,10,17]. In brief from this table, in addition to the design simplicity, the inverted arm topology is advantageous in terms of attenuation loss, access matching and the NGD absolute value.

Reference	f_n	GD_n	BW	$S_{21}(f_n)$	$S_{11}(f_n)$
[1]	4.5 GHz	-50 ps	3 GHz	-9 dB	-
[8]	1.99 GHz	-2.1 ns	440MHz	-2.5 dB	-
[9]	1.016 GHz	-2.09 ns	44 MHz	-18.1 dB	33 dB
[10]	2.3 GHz	-2 ns	36 MHz	-3.4 dB	-10 dB
[17]	1.79 GHz	−7.7 ns	35 MHz	-8.6 dB	-20 dB
This work	3.604 GHz	-8.699 ns	3.3 MHz	-1 dB	-20 dB

Table 4: Comparison of BP NGD performances.

4. Conclusion

An original modelling approach of BP NGD topology based on identical parallel lines with inverted arms is investigated. The distributed NGD structure is composed of TL elements. The S-matrix model is established innovatively in function of the constituting

element characteristic impedance and propagation constant. The expressed model is validated with a microstrip inverted arm circuit. As expected, calculated and simulated BP NGD functions were in very good correlation. It is important to note from the study that the NGD effect can be generated with parallel arm structures via permutation of the constituting elements. In the continuation of this study, inverted arm-based BP NGD circuits designed operating in multi-band and tunable NGD can be potentially implemented in communication system to face up the issue related to the GD.

5. References

[1] C. D. Broomfield and J. K. A. Everard, “Broadband Negative Group Delay Networks for Compensation of Oscillators, Filters and Communication Systems,” Electron. Lett., Vol. 36, No. 23, pp. 1931-1933, Nov. 2000.

[2] T. Zhang, R. Xu and C. M. Wu, “Unconditionally Stable Non-Foster Element Using Active Transversal-Filter-Based Negative Group Delay Circuit,” IEEE Microw. Wireless Compon. Lett., vol. 27, no. 10, pp. 921-923, Oct. 2017.

[3] B. Ravelo, S. Lalléchère, A. Thakur, A. Saini and P. Thakur, “Theory and circuit modelling of baseband and modulated signal delay compensations with low- and band-pass NGD effects”, Int. J. Electron. Commun. (AEÜ), Ed. Elsevier, Vol. 70, No. 9, Sept. 2016, pp. 1122–1127.

[4] T. Shao, Z. Wang, S. Fang, H. Liu and Z. Chen, “A Full-Passband Linear-Phase Band-Pass Filter Equalized with Negative Group Delay Circuits,” IEEE Access, vol. 8, Feb. 2020, pp. 43336-43343.

[5] S. Chu and S. Wong, “Linear Pulse Propagation in an Absorbing Medium,” Phys. Rev. Lett., Vol. 48, 1982, pp. 738-741.

[6] B. Ségard and B. Macke, “Observation of Negative Velocity Pulse Propagation,” Phys. Lett. A, Vol. 109, pp. 213-216, 1985.

[7] B. Ségard and B. Macke, “Two-pulse interference and superluminality,” Optics Communications, vol. 281, no. 1, pp. 12–17, Jan. 2008.

[8] B. Ravelo, “Negative Group-Delay Phenomenon Analysis with Distributed Parallel Interconnect Line”, IEEE Transactions on Electromagnetic Compatibility, Vol. 58, No. 2, Apr. 2016, pp. 573-580.

[9] Z. Wang, Y. Cao, T. Shao, S. Fang and Y. Liu, “A Negative Group Delay Microwave Circuit Based on Signal Interference Techniques,” IEEE Microw. Wireless Compon. Lett., vol. 28, no. 4, pp. 290-292, Apr. 2018.

[10] F. Wan, N. Li, B. Ravelo, Q. Ji and J. Ge, “S-Parameter Model of Three Parallel Interconnect Lines Generating Negative Group-Delay Effect,” IEEE Access, Vol. 6, No. 1, Dec. 2018, pp. 57152-57159.

[11] B. Macke and B. Ségard, “Propagation of light-pulses at a negative group-velocity,” Eur. Phys. J. D, vol. 23, pp. 125–141, 2003.

[12] O. F. Siddiqui, M. Mojahedi and G. V. Eleftheriades, “Periodically Loaded Transmission Line with Effective Negative Refractive Index and Negative Group Velocity,” IEEE Trans. Antennas Propagat., Vol. 51, No. 10, Oct. 2003, pp. 2619-2625.

[13] L. Markley and G. V. Eleftheriades, “Quad-Band Negative-Refractive-Index Transmission-Line Unit Cell with Reduced Group Delay,” Electronics Letters, Vol. 46, No. 17, Aug. 2010, pp. 1206-1208.

[14] L.-F. Qiu, L.-S. Wu, W.-Y. Yin, and J.-F. Mao, “Absorptive bandstop filter with prescribed negative group delay and bandwidth,” IEEE Microw. Wireless Compon. Lett., vol. 27, no. 7, pp. 639-641, Jul. 2017.

[15] H. Choi, Y. Jeong, J. Lim, S. Y. Eom, and Y. B. Jung, “A novel design for a dual-band negative group delay circuit,” IEEE Microw. Wireless Compon. Lett., vol. 21, no. 1, pp. 19–21, Jan. 2011.

[16] G. Chaudhary, Y. Jeong and J. Lim, “Miniaturized dual-band negative group delay circuit using dual-plane defected structures,” IEEE Microwave Wireless Compon. Lett., vol. 24, no. 8, pp. 521-523, Aug. 2014.

[17] G. Liu and J. Xu, “Compact transmission-type negative group delay circuit with low attenuation,” Electron. Lett., vol. 53, no. 7, pp. 476-478, Mar. 2017.

[18] T. Shao, Z. Wang, S. Fang, H. Liu, and S. Fu, “A compact transmission line self-matched negative group delay microwave circuit,” IEEE Access, vol. 5. pp. 22836-22843, Oct. 2017.

[19] T. Shao, S. Fang, Z. Wang and H. Liu, “A Compact Dual-Band Negative Group Delay Microwave Circuit,” Radio engineering, vol. 27, no. 4, pp. 1070-1076, Dec. 2018.

[20] B. Ravelo, “On the low-pass, high-pass, bandpass and stop-band NGD RF passive circuits”, URSI Radio Science Bulletin, Vol. 2017, No. 363, Dec. 2017, pp. 10-27.

[21] B. Ravelo, “Similitude between the NGD function and filter gain behaviours”, Int. J. Circ. Theor. Appl., Vol. 42, No. 10, Oct. 2014, pp. 1016–1032.

[22] B. Ravelo, “First-order low-pass negative group delay passive topology,” Electronics Letters, Vol. 52, No. 2, Jan. 2016, pp. 124–126.

[23] R. Randriatsiferana, Y. Gan, F. Wan, W. Rahajandraibe, R. Vauché, N. M. Murad and B. Ravelo, “Study and Experimentation of a 6-dB Attenuation Low-Pass NGD Circuit,” Analog. Integr. Circ. Sig. Process., pp. 1-14, Apr. 2021.

[24] R. Yang, X. Zhou, S. Yazdani, E. Sambatra, F. Wan, S. Lalléchère and B. Ravelo, “Analysis, design and experimentation of high-pass negative group delay lumped circuit,” Circuit World, Aug. 2021, pp. 1-25.

[25] F. Wan, X. Huang, K. Gorshkov, B. Tishchuk, X. Hu, G. Chan, F. E. Sahoa, S. Baccar, M. Guerin, W. Rahajandraibe and B. Ravelo, “High-pass NGD characterization of resistive-inductive network based low-frequency circuit,” COMPEL - The International Journal for Computation and Mathematics in Electrical and Electronic Engineering, Vol. 40, No. 5, pp. 1032-1049, 2021.

[26] G. Chaudhary, and Y. Jeong, “Tunable center frequency negative group delay filter using coupling matrix approach,” IEEE Microwave Wireless Component Letters, Vol. 27, No. 1, 2017, pp. 37-39.

[27] S. Ngoho, Y. C. M. Boussougou, S. S. Yazdani, Y. Dong, N. M. Murad, S. Lalléchère, W. Rahajandraibe and B. Ravelo, “Design and modelling of ladder-shape topology generating

bandpass NGD function," Progress In Electromagnetics Research (PIER) C, Vol. 115, pp. 145-160, 2021.

[28] E. Hammerstad and O. Jensen, "Accurate Models for Microstrip Computer-Aided Design," 1980 IEEE MTT-S International Microwave Symposium Digest, Washington, DC, USA, 1980, pp. 407-409, doi: 10.1109/MWSYM.1980.1124303.